Tkac, O., Saha, A. K., Onvlee, J., Yang, C-H., Sarma, G., Bishwakarma, C. K., ... Orr-Ewing, A. J. (2013). State-to-state resolved differential cross sections for rotationally inelastic scattering of ND3 with He. Physical Chemistry Chemical Physics, 16(2), 477-488. 10.1039/c3cp53550a

PCCP

Dynamic Article Links ►

Cite this: DOI: 10.1039/c0xx00000x

www.rsc.org/xxxxxx

PAPER TYPE

State-to-state resolved differential cross sections for rotationally inelastic scattering of ND_3 with He.

Ondřej Tkáč,[a] Ashim Kumar Saha,[b] Jolijn Onvlee,[b] Chung-Hsin Yang,[b] Gautam Sarma,[b] Chandan Kumar Bishwakarma,[b] Sebastiaan Y.T. van de Meerakker,[b] Ad van der Avoird,*[b] David H. Parker*[b], and Andrew J. Orr-Ewing*[a]

Received (in XXX, XXX) Xth XXXXXXXXX 20XX, Accepted Xth XXXXXXXXX 20XX

DOI: 10.1039/b000000x

State-to-state differential cross sections are reported for rotationally inelastic scattering of fully state-selected ND_3 ($j_k^{\pm} = 1_1^-$) with He. Experimental measurements are compared with full close-coupling quantum-mechanical scattering calculations that used an *ab initio* potential energy surface. Results are presented for final states up to $j'^{\pm}_{k'} = 7_7^-$ at a mean collision energy of 430 cm^{-1}. For selected final quantum states, the effect of collision energy on the differential cross sections is also explored in the range 230 – 720 cm^{-1}. For the experimental studies, a hexapole electrostatic lens was used for the $j_k^{\pm}$ state-selection of ND_3 molecules in their electronic and vibrational ground states in a molecular beam. This state-selected molecular beam was then crossed with a beam of He atoms. The velocities of inelastically scattered ND_3 molecules in single $j'^{\pm}_{k'}$ states were obtained by velocity map imaging, and converted to differential cross sections in the centre-of-mass frame by density-to-flux transformation. The close-coupling calculations reproduce well the measured angular distributions. For small changes in the rotational angular momentum quantum number (j), the ND_3 is predominantly forward scattered, but the scattering shifts to the sideways and backward directions as Δj increases. For scattering into a given $j'^{\pm}_{k'}$ state, cross-sections for collisions that conserve the +/- symmetry associated with the ND_3 inversion vibration are larger and generally more forward scattered than the corresponding symmetry-changing processes.

I. Introduction

The study of rotational energy transfer in collisions of ammonia isotopologues was originally motivated by astrophysical applications, especially to aid the interpretation of NH_3 radio frequency signals.[1, 2] The discovery of ammonia in the interstellar medium dates back to 1968,[3] when emissions were observed at a frequency corresponding to the inversion transitions of the rotational levels j_k = 1_1 and 2_2 in the vibrational ground state of NH_3. Since then, ammonia has been observed in various environments, such as comets,[4] the Galactic centre,[5] the T dwarf class of brown dwarf stars,[6] and in diffuse and translucent molecular clouds.[7] Ammonia is also present in the Earth's troposphere,[8] and has been identified in the atmospheres of extrasolar planets.[9] Fully deuterated ammonia, ND_3, has been observed in prestellar cores.[10] Cheung *et al.*[11] noted that the observed NH_3 emission intensities from interstellar sources do not correspond to a single rotational temperature. In addition, the inversion transition was detected for the rotational level $j_k = 11_9$,[12] which should not be populated at interstellar temperatures of 10-300 K, and the $j_k = 3_3$ inversion transition has been predicted[13] and observed[14] to exhibit maser activity. These observations clearly showed that the emitting NH_3 is not in thermal equilibrium with its environment.

Because gas-phase collisions can transfer population to higher-lying rotational levels, inelastic scattering experiments help interpret the anomalous non-thermal microwave radiation emitted from interstellar clouds.[15, 16] An important goal of scattering experiments is to determine the state-to-state differential cross section (DCS), $d\sigma/d\Omega(\theta, E, i \rightarrow f)$, which captures the variation of the scattering cross section for a change from initial state i to final state f as a function of the centre-of-mass (CM) scattering angle θ for a specified collision energy E. The DCS is expressed visually in the form of the surface distribution of particles on an expanding velocity sphere, a so-called Newton sphere. In our work we measure these Newton spheres experimentally as product density spheres and convert them to the desired product flux spheres. From these flux spheres, we extract the desired state-to-state DCSs, and compare these DCSs with those predicted from calculations carried out on highly accurate potential energy surfaces (PESs). These same surfaces are used to derive rate constants for astrochemical models. From the state-to-state DCSs that we compute, the integral state-to-state cross section $\sigma(E, i \rightarrow f)$ can be derived by integration over all scattering angles, and can also be used to calculate the thermal rate constants.

In addition to astrochemical motivations, the study of ammonia collisions is becoming a hot topic in the cold molecule field. Slow collisions of NH_3 molecules with He atoms were studied theoretically by Gubbels *et al.*[17] who described the strong effects of scattering resonances on state-to-state integral cross sections (ICSs) as well as DCSs for collision energies ranging from 10^{-4} cm^{-1} to 130 cm^{-1}. While work in the Nijmegen laboratory on cold collisions is presently ongoing, this paper describes collisions of ND_3 with He for higher energy where smooth trends in the DCSs and ICSs are expected.

Inelastic collisions of NH_3 with He[16, 18, 19] have been the subject of extensive previous study, with an emphasis on

determination of ICSs and collision rates. However, experimental and theoretical DCSs were also reported for this system, [18, 19] although, with the exception of calculations presented in Ref [18], without selection of the inversion symmetry of the initial state associated with the umbrella vibrational mode. These measurements of DCSs for NH_3 collisions are complemented in the current study by detailed investigation of the scattering of ND_3 molecules in collisions with He. The ND_3 rotational energy levels are more closely spaced than those for NH_3 because of differences in the rotational constants for the isotopologues. Therefore, a collision induced transition into the same final state of scattering is accompanied by an approximately two fold greater energy transfer for NH_3 than for ND_3. In this way, we can explore whether the dynamics of collisions are controlled by changes in the rotational quantum numbers j and k or in the total transferred energy. The ND_3 – collider system also has greater reduced mass than the NH_3 – collider system, so the dynamics evolving on the PES may be expected to differ. For example, from the classical results for rotational rainbow scattering of a homonuclear molecule with an atom,[20] the position of the rotational rainbow for a given j and collision energy is expected to shift towards larger scattering angles for the deuterated system.[21]

The current work seeks to explore the dynamics of translational to rotational energy transfer in collisions of He with ND_3 and therefore to understand better the intermolecular interactions between these species. Measurements are reported of quantum-state resolved DCSs obtained using crossed molecular beam (CMB) scattering,[22-24] combined with resonance enhanced multi-photon ionization (REMPI) detection and velocity-map imaging (VMI).[25] At this level of resolution of the dynamics of a scattering process, rigorous comparisons can be drawn between experimental measurements and the outcomes of quantum mechanical (QM) scattering calculations. Such comparisons provide stringent tests of the accuracy of *ab initio* computed PESs for the collisional processes of interest. Although there is a significant body of work on inelastic scattering of diatomic molecules, such detailed experimental and computational investigations for scattering of polyatomic molecules remain relatively rare.[26]

A number of PESs have been developed previously for the NH_3 – He[2, 27-32] scattering system. In addition, theoretical DCSs for this system were reported by Meyer *et al.*[29] using the coupled state approximation and by van der Sanden *et al.*[18] using close coupling methods with empirical and scaled *ab initio* potential energy surfaces.

In this paper, results are presented for the state-to-state scattering of ND_3 in its ground electronic ($\tilde{X}^1A_1'$) and vibrational ($v = 0$) levels from He:

$$ND_3\ (\tilde{X}, v = 0, j_k^{\pm} = 1_1^-) + He \rightarrow ND_3\ (\tilde{X}, v' = 0, j'^{\pm}_{k'}) + He$$

with $j' \leq 7$, $k' \leq 7$, and +/– denoting symmetry / anti-symmetry of the inversion state associated with the v_2 umbrella vibrational mode. Initial state selection is achieved by passing a supersonically expanded and cooled molecular beam of ND_3 in an inert carrier gas through a hexapole state selector prior to intersection with a secondary beam of He. REMPI detection of individual $j'^{\pm}_{k'}$ levels of ND_3 allows determination of the relative density of scattering into all angles (defined with respect to the relative velocity of the ND_3 molecule in the CM frame), and, via density-to-flux transformation, fully state-to-state DCSs are obtained. Experimental measurements are contrasted with QM scattering calculations performed on a recently derived PES.

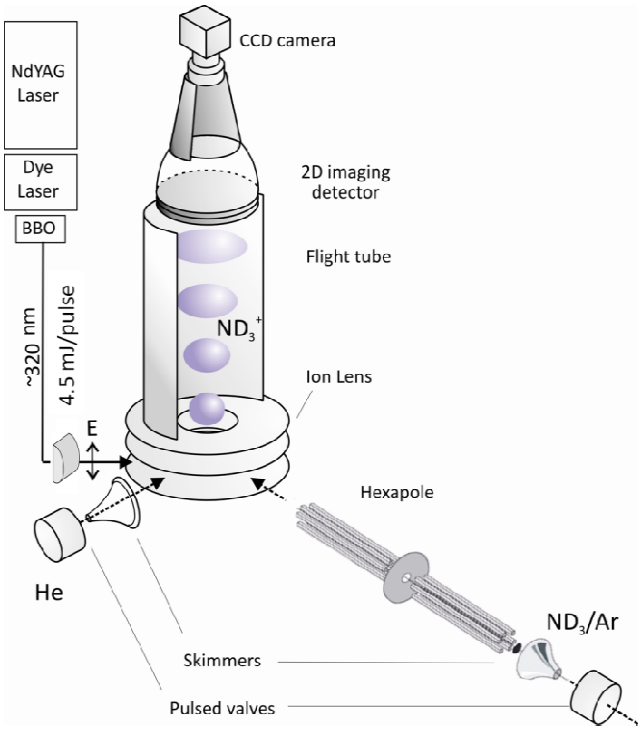

Fig. 1 Schematic diagram of the crossed molecular beam and VMI apparatus

II. Method

A. Experimental apparatus

The experimental measurements were performed in a crossed-beam scattering machine located in the Nijmegen laboratory and shown schematically in Figure 1. Beams of ND_3 (seeded in a carrier gas) and the collider gas intersected at 90° within a high vacuum chamber, and ND_3 molecules scattered into various $j'^{\pm}_{k'}$ rotational levels were detected with rotational level and inversion symmetry resolution using REMPI and VMI. The velocity map images contain information on the angular variation of the density of scattered ND_3 molecules, and image analysis to determine state-resolved DCSs requires careful characterization of various experimental parameters. Further details of the procedures and outcomes of the necessary density-to-flux transformation are presented in section C.

The primary molecular beam was produced by supersonic expansion of a mixture of 1% ND_3 seeded in argon, krypton or xenon at a backing pressure of 2 bar through a home-built Nijmegen pulsed valve.[33] The secondary helium beam resulted from expansion of the pure gas (1 bar backing pressure) through a hairpin-type Jordan pulsed valve placed in a differentially pumped source chamber. Both valves had opening times of ~100 µs and operated at repetition rates of 10 Hz. The expansions were collimated by skimmers (3-mm diameter) located 30 mm

from the valve orifices. The primary beam of ND_3 molecules then either passed through a pair of 12 cm long hexapoles operating at 18.5 kV if initial state selection was required, or a different source chamber was used without hexapole focusing. Distances from the entrance of the skimmer to the scattering centre were 5 cm for the secondary beam, and 31 cm (with the hexapole) or 5.5 cm (without hexapole focusing) for the primary beam. The two beams intersected at 90° inside the collision chamber, which was maintained at a pressure of 2×10^{-6} mbar during experimental measurements and had a base pressure (with the pulsed valves turned off) of $\sim 3 \times 10^{-7}$ mbar.

Collisions between particles in the primary and secondary beams occurred at the centre of an electrode assembly designed for velocity map imaging. ND_3 was state-selectively ionized by (2+1) REMPI via the ν_2 = 4 or 5 vibrational levels of the $\tilde{B}$ Rydberg electronic state using respective ultraviolet wavelengths of 321-322 nm and 317-318 nm. These wavelengths were generated by frequency doubling the output of a tuneable pulsed dye laser (Lambda Physik ScanMate) operating with DCM dye using a BBO doubling crystal. The dye laser was pumped by a Nd:YAG laser (Continuum Powerlite 9000) operating at 532 nm and with 10 Hz repetition rate. Typical ultraviolet (UV) laser energies were ~4.5 mJ/pulse in pulses of duration 7-9 ns. A 50 cm or 20 cm focal length spherical lens was used to focus the ionization laser into the scattering centre, and the diameter of the beam spot on the lens was 2 mm. The laser propagation direction was parallel to the relative velocity vector for experiments performed with the hexapole, and perpendicular to the relative velocity for experiments without the hexapole.

Current experiments were performed with a fixed wavelength chosen to give maximum scattering signal, rather than scanning the wavelength over the full width of the Doppler profile of the REMPI transition (0.1 cm^{-1} for inelastic scattering of ND_3 from He). However, the laser bandwidth was ~0.3 cm^{-1} and the ~4.5 mJ energy per pulse of the laser power broadened the transitions sufficiently that Doppler scanning was unnecessary.

The expanding Newton sphere of ND_3^+ ions prepared by REMPI of scattered ND_3 was extracted by static electric fields toward the VMI detector, which consisted of a pair of position sensitive microchannel plates (MCPs) located in front of a phosphor screen viewed by a CCD camera synchronized with the UV laser pulses. The laser also created ions with other masses, so the detector was switched on only for a short period of time to detect only those ions with the desired mass-to-charge ratio. In all the experimental results presented here, images were recorded as a two dimensional projection of the Newton sphere of ions. Position and intensity data from the CCD camera were transferred to a PC for further processing and analysis.

The VMI ion optics consisted of a repeller, an extractor, and a grounded electrode, all of diameter 80 mm. The separations between repeller and extractor plate and between extractor and ground plates were, respectively, 10 and 15 mm, with a repeller voltage of 1 kV, and optimization of the extractor voltage to ±3 V around 777 V to ensure circular and focused images. The radius of the recorded ion image is then directly proportional to the CM-frame speed of the ions at their point of formation by REMPI. For the ionization schemes employed here, the recoil of the electron from the ion (deriving from the excess energy of three UV photons above the 10.08 eV[34, 35] ionization energy of ND_3) can impart up to 20 ms^{-1} to the ND_3^+ corresponding to an ~3 pixel blurring of the images.[36]

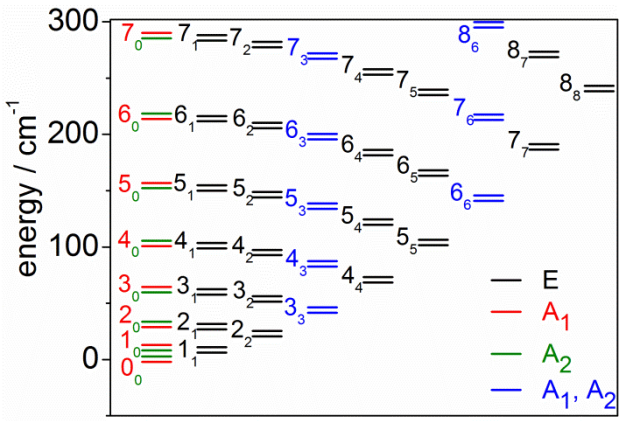

Fig. 2 Rotational energy level diagram for the $\tilde{X}(\nu_2 = 0)$ state of ND_3. Levels are labelled by j_k rotational quantum numbers and are split into +/– symmetries of the umbrella vibrational mode. This splitting is exaggerated for clarity. The levels corresponding to the individual nuclear spin modifications are indicated.

Table 1 Populations (given in percent of the total population) of the ND_3 rotational levels in the incident molecular beam at a rotational temperature of 4 K.

Rotational level $j_k^{\pm}$	ND_3
0_0^-	3.5
0_0^+	34.4
1_1^-	29.1
1_1^+	29.6
1_0^-	2.6
1_0^+	0.2

B Rotational levels and initial state selection of ND_3

Ammonia in the ground state has a pyramidal (C_{3v}) equilibrium geometry.[37] The double-minimum potential along the inversion coordinate associated with the ν_2 "umbrella" vibrational mode of ammonia gives rise to a splitting of all rotational levels into doublets with symmetric and antisymmetric components denoted by + and – respectively. ND_3 is a symmetric top and its rotations are described by the usual angular momentum and projection quantum numbers j and k. Figure 2 depicts a rotational energy level diagram of the $\tilde{X}(\nu_2 = 0)$ state of ND_3. The ND_3 molecule exists in three nuclear spin modifications. The A_1 nuclear spin functions are associated with rotational levels with k = 0 and odd j and with levels for which k is a multiple of 3. The A_2 nuclear spin function corresponds to rotational levels with even j and k = 0, and also to levels for which k is a multiple of 3. Therefore, the rotational levels with k = 3, 6, … have both A_1 and A_2 components of the same energy. The E nuclear spin functions include all levels for which k is not a multiple of 3. The ND_3 cannot inter-convert between different nuclear spin modifications during collisions. Therefore, initial state selection of the 1_1^- level, as discussed below, limits the final states that can be

observed in our experiments to those of *E* symmetry.

Initial state preparation of ND_3 consisted first of rotational cooling during the adiabatic expansion, followed by quantum state selection in a hexapole electrostatic field. A measured REMPI spectrum of ND_3 via the $\tilde{B}(\nu_2 = 5)$ state, when compared to a simulated spectrum using the PGOPHER program,[38] revealed a rotational temperature of 4 K. The relative populations at this temperature are shown in Table 1. Only the three lowest energy rotational levels j_k = 0_0, 1_1 and 1_0 are significantly populated, with just 0.7% of population in the higher rotational levels. The cooled ND_3 molecules were subjected to hexapole electrostatic state selection, in which states with $k \neq 0$ experience a radial force due to an interaction of the electric field with the molecular dipole moment. The direction of this force depends on the parity of the molecular state: molecules with symmetric umbrella inversion (+) diverge from the path along the hexapole axis, whereas molecules with antisymmetric inversion symmetry (–) experience a restoring force and are focussed into the scattering region.

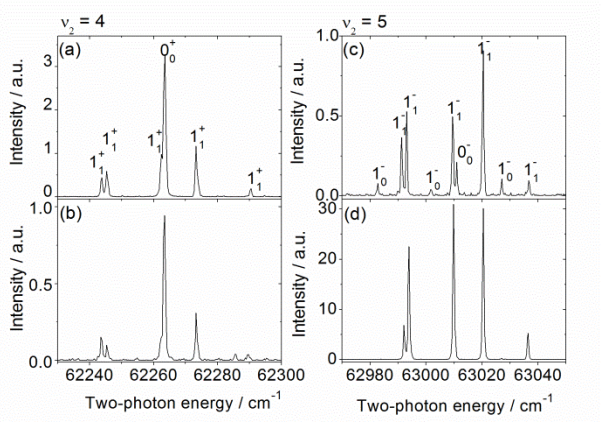

Fig. 3 REMPI spectra of ND_3 in the primary molecular beam: (a) without and (b) with hexapole state selection, with excitation via the $\tilde{B}(4)$ band; (c) without and (d) with hexapole state selection, with excitation via the $\tilde{B}(5)$ band. Labels indicate the j_k rotational quantum numbers and umbrella vibration inversion symmetry of the levels from which the transitions originate.

Molecules prepared in the well-defined initial state $j_k^{\pm} = 1_1^-$ are excited by collisions with He into various final rotational states, most of which lie higher in energy, and velocity map images were obtained for various $j'^{\pm}_{k'}$ levels using the well-known (2+1) REMPI of ND_3 via the 2-photon $\tilde{B} \leftarrow \tilde{X}$ transition.[39-41] One consequence of symmetry and nuclear spin constraints is that only transitions originating from the lower (+) inversion component of the ground state appear in bands in which the final ν_2 is even, whereas only transitions from the upper (–) inversion component appear in bands with final ν_2 odd. Therefore, two vibrational transitions must be excited to probe all individual rotational states. The $\tilde{B}(\nu_2 = 4) \leftarrow \tilde{X}(\nu_2 = 0)$ transition at wavelengths near 321 nm probes ND_3 states with + inversion symmetry populated by the scattering, while – inversion symmetry of the final scattering states is probed by the $\tilde{B}(\nu_2 = 5) \leftarrow \tilde{X}(\nu_2 = 0)$ transition at wavelengths around 317 nm.

Figure 3 shows the rotational REMPI spectra of non-scattered ND_3 molecules in the primary beam, measured with and without hexapole state selection, for 2-photon excitation via the ν_2 = 4 and 5 vibrational levels of the $\tilde{B}$ state. Note the deflection of molecules in the 1_1^+ state causes a decrease in intensity of the $\tilde{B}(4)$ transitions when using the hexapole, but the hexapole focusing of the 1_1^- levels into the scattering centre considerably enhances signals in the spectrum obtained via the $\tilde{B}(5)$ state.

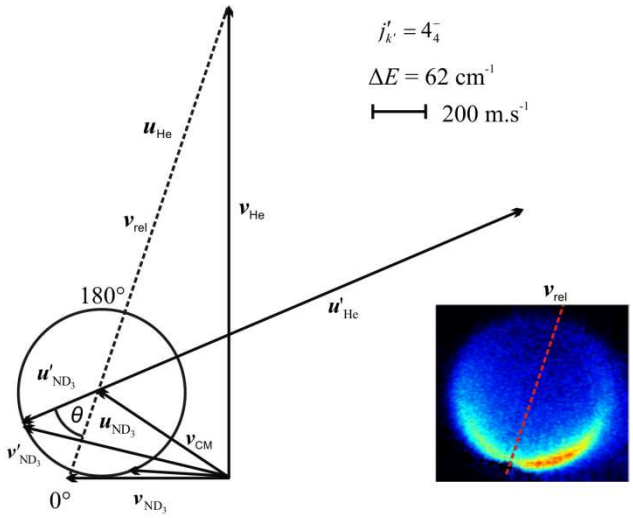

Fig. 4 Newton diagram for inelastic scattering of ND_3 with helium from $j_k^{\pm} = 1_1^-$ to the 4_4^- level. The orientation corresponds to the experimental arrangement using the hexapole focusing. For experiments without the hexapole state selector, the Newton diagram is the same, but reflected about the $\mathbf{v}_{He}$ vector.

In the $\tilde{B}(5)$ band, the intensities of the 1_0^- lines are the same for measurement with and without hexapole state selection, although these lines are hardly visible in the spectrum obtained with hexapole state selection because of the larger ordinate scale. The 0_0^+ line is not visible in the spectrum measured with the hexapole because it is overlapped by a much stronger 1_1^- line. REMPI lines originating from levels with k = 0 are not enhanced because, as noted earlier, k = 0 states are not focused by the hexapole.[16]

Therefore, experiments combining rotational cooling in a pulsed expansion and subsequent hexapole focusing concentrate only on scattering of state-selected $ND_3(1_1^-)$ to other *E* symmetry levels. Scattering of any residual 0_0^+ population present in the beam does not play any role in experiments probing *E*-symmetry product levels since the 0_0^+ state has A_2 symmetry. However, ND_3 molecules in the 1_1^+ level also have *E* symmetry and can contribute to our inelastic scattering signals, but are present at ≤1 % of the 1_1^- population after state selection and so can be neglected. State-specific REMPI detection of scattered products then allows measurements of true state-to-state scattering.

C Density-to-flux transformation to derive differential cross sections

A Newton diagram for inelastic scattering of ND_3 with He is displayed in Figure 4 together with a typical image obtained in the experiment. The figure shows the laboratory frame velocities of ND_3, $\boldsymbol{v}_{ND_3}$, and helium, $\boldsymbol{v}_{He}$, and their pre- and illustrative post-collision centre-of-mass frame velocities, $\boldsymbol{u}_{ND_3}$, $\boldsymbol{u}_{He}$ and, $\boldsymbol{u}'_{ND_3}$, $\boldsymbol{u}'_{He}$ respectively. The Newton sphere of ions moves in the

laboratory frame with CM velocity, $\boldsymbol{v}_{\mathrm{CM}}$. The CM-frame scattering angle, θ, is defined as the angle between the CM-frame velocities of ND_3 before and after a collision. For the discussion of the density-to-flux transformation that follows, the figure shows a pair of laboratory frame velocities for ND_3 molecules after collision, $\boldsymbol{v}'_{\mathrm{ND_3}}$ that have the same CM-frame scattering angle. The intensities at these points in the velocity image should be the same. However, the image clearly shows that intensity around the point with smaller laboratory frame velocity is larger than around the point with larger laboratory frame velocity. In general the measured image should be symmetric with respect to the relative velocity vector, $\boldsymbol{v}_{\mathrm{rel}}$(dashed line). The asymmetry in the image results from bias in the detection of products with different laboratory speeds.

The primary and secondary molecular beams overlap for periods on the order of ~100 μs and scattering products that are more slowly moving in the laboratory frame (because their CM-frame velocities oppose the velocity of the CM) are more likely to lie within the volume probed by the much shorter duration laser pulse than are faster moving scattering products. This detection bias leads to an asymmetry about the relative velocity vector in raw images that can be corrected with careful consideration of speed-dependent experimental detection probabilities to derive true CM frame angular scattering distributions.

The asymmetry about the relative velocity vector also prevents reconstruction of the three-dimensional (3D) Newton sphere of scattering velocities from the two-dimensional (2D) experimental projections using standard techniques such as the inverse Abel transform. In the current work, we tested both McBane's iterative extraction method IMSIM[42] (IMage SIMulation, based on the repeated comparison of a simulated image with the experimental image), and the method of Monte Carlo simulation of the experiment, using a modification of the computer program of Eyles and Brouard.[43] Both codes provide density-to-flux transformation of experimental images, so that DCSs can be extracted. For both programs, values for various parameters describing features of the experimental apparatus have to be included, and these were carefully determined.

We express the measured raw image ($N_{image}(\theta)$), which is proportional to the number density, as a product of the DCS and an angle-dependent instrument function ($G_{Inst}(\theta)$) which incorporates the LAB-speed (and thus CM-frame scattering angle) dependent detection probabilities:

$$N_{image}(\theta) = \frac{\mathrm{d}\sigma}{\mathrm{d}\Omega} G_{Inst}(\theta). \qquad (1)$$

The desired DCSs, $\frac{\mathrm{d}\sigma}{\mathrm{d}\Omega}$, can then be determined by dividing an experimental image by a synthetic image of the instrument function, which is generated from a simulation employing a perfectly isotropic DCS in the CM frame. The IMSIM and Monte Carlo methods for generating these instrument functions have been described in detail elsewhere.[43-48] Here, we focus on the determination of key parameters that are input to these codes to account for the conditions specific to our experimental set up.

For reliable use of both the IMSIM and Monte Carlo simulation programs, we carefully characterized the speed and angular divergence distributions, temporal profiles, and spatial widths of the two molecular beams, as well as the temporal profile, Rayleigh range and beam waist of the focused probe laser. These latter parameters, which can be calculated from the focal length of the spherical lens and the diameter of the beam spot on the lens, determine the location-dependent probability of inducing a 2-photon excitation to the $\tilde{B}$-state. The speed distributions of the molecular beams were measured by positioning the pulsed valves at various distances from the scattering centre and determining the time of arrival using REMPI detection. The angular divergence distributions and spatial widths of the two molecular beams were calculated from the geometrical arrangement, using known nozzle and skimmer diameters and nozzle-to-skimmer and skimmer-to-scattering centre distances. The temporal profiles of the molecular beams were measured by changing the delay time between opening of the nozzles and firing of the laser, using unscattered ND_3 REMPI signals. The FWHMs of the measured distributions were then used in the Monte Carlo and IMSIM simulation programs with the assumption that the temporal profiles of the pulsed molecular beams were Gaussian. For a given velocity map image and set of experimental parameters, the Monte Carlo and IMSIM programs generated almost identical DCSs, so the majority of the results presented hereafter have been analysed using only the Monte Carlo image processing method. The exceptions to this are the results presented in Section III.D, for which the IMSIM analysis code was preferred because it allows for changes to the geometry of the CMB experiment.

By sampling ~2×10^8 sets of initial conditions from the distributions of molecular beam and laser beam properties, the Monte Carlo program was used to assemble a position and speed dependent detection probability function corresponding to $G_{Inst}(\theta)$ for use in equation (1). Because of imperfect alignment and focusing by the hexapole, the primary beam was displaced ~3 mm away from the centre of the electrostatic imaging lens. REMPI detection at the centre of the crossing region of the molecular beams therefore led to slight image distortion and higher background, so detection was carried out by laser ionization at the centre of the imaging ion optics and corrections for the molecular beam misalignment were incorporated into the density-to-flux conversion routine. The non-parity selected (*i.e.*, without the hexapole) experiments did not need this correction.

D. Quantum scattering calculations

Integral and differential state-to-state cross sections were computed by close-coupling calculations. These calculations were performed using the intermolecular PES of Gubbels *et al.*[17] for NH_3-He. This PES is based on an analytic fit of 4180 data points computed with the CCSD(T) method and an AVQZ basis set in the long range, and with the CCSD(T)-F12 method and an AVTZ basis set including mid-bond functions in the short range. The interaction potential is described in terms of four coordinates: R, β, γ, and ρ, where R is the length of the vector $\boldsymbol{R}$ that points from the centre-of-mass of the NH_3 molecule to the He atom. The angles β and γ are the zenith and azimuthal angles of the three-fold (C_{3v}) symmetry axis of NH_3 in a body-fixed dimer frame with its z-axis parallel to $\boldsymbol{R}$. The umbrella or inversion angle ρ of the NH_3 molecule is defined as the angle

between the symmetry axis of the molecule and a vector pointing from the N atom to one of the H atoms, so that $\rho = \pi/2$ corresponds to a planar NH_3 geometry.

The present study concerns ND_3 rather than NH_3. These isotopologues have the same electronic structure and we assume them to have the same geometry, which implies that the NH_3-He and ND_3-He interaction potentials are identical. However, when NH_3 is replaced by ND_3 the monomer centre-of-mass shifts along the three-fold symmetry axis of the molecule and the intermolecular coordinates are different. The new coordinates R' and β' valid for ND_3-He can easily be expressed in terms of the NH_3-He coordinates R and β, whereas the coordinates γ and ρ do not change.

The interaction potential of NH_3-He was expanded in tesseral harmonics (real-valued spherical harmonics) depending on β and γ; the expansion coefficients depend on R and ρ.[17] When NH_3 is replaced by ND_3, the coordinates are shifted and we had to make a new expansion for the ND_3-He potential with tesseral harmonics in the angles β' and γ and the expansion coefficients depending on R' and ρ. The new expansion coefficients were calculated by numerical quadrature after computing the ND_3-He potential on a Gauss-Legendre grid with 11 values of β' in the range from 0 to π and an equidistant Gauss-Chebyshev grid for γ with the points $\pi/24$, $3\pi/24$, $5\pi/24$, and $7\pi/24$. The grid for γ could be restricted to the range $0 \le \gamma \le \pi/3$ because of the C_{3v} symmetry of the molecule. The computation of the expansion coefficients was performed for the equidistant radial grid of 212 points from $R' = 4$ to 40 a_0 that was used by the renormalized Numerov propagator applied in the scattering calculations. The ρ dependence of the NH_3-He potential was obtained by polynomial fits of the expansion coefficients calculated for five equidistant grid points centered at $\rho_3 = 0.6226\pi$ with step size $\Delta\rho = (2\rho_3 - \pi)/5$.[17] The expansion coefficients of the ND_3-He potential used here were obtained similarly. To obtain the actual values of the ND_3-He potential on the grid we expressed the grid values of R' and β' in terms of the NH_3-He coordinates R and β and computed the NH_3-He potential from its analytical form given in Ref. 17.

In the NH_3-He scattering calculations of Gubbels *et al.*[17] the ammonia umbrella (inversion) motion was treated by two different methods. In the first method the umbrella vibration-inversion wave functions and energy levels of the NH_3 monomer were computed numerically in a double-well potential depending on the coordinate ρ; this potential was chosen such that the calculated vibrational $\nu_2 = 0 \rightarrow 1$ excitation energy and the inversion splittings of the $\nu_2 = 0$ and $\nu_2 = 1$ levels agreed with the experimental values. The curvilinear umbrella motion was correctly taken into account in the ρ dependent kinetic energy operator. Here, we apply the same method to the ND_3 monomer with the use of the experimental data for ND_3.[49] The ground state inversion tunneling splitting of 0.0530 cm^{-1} in ND_3 is 15 times smaller than the corresponding splitting of 0.7934 cm^{-1} in NH_3. The lowest four ammonia vibration-inversion states were explicitly included in the NH_3-He scattering calculations[17] as well as in the present work for ND_3-He.

The other method used to include the ammonia inversion motion in the NH_3-He scattering calculations was by the use of a two-state model.[17] This model approximates the $\nu_2 = 0$ inversion tunneling states of the ammonia monomer as an even and odd combination of the two rigid equilibrium structures. The ρ dependence of the intermolecular potential is not used in this method; only the potential for the equilibrium umbrella angle ρ_e is needed. This model is implemented in our scattering program and it was used in most of the calculations described here. In order to test its accuracy a few calculations were also performed

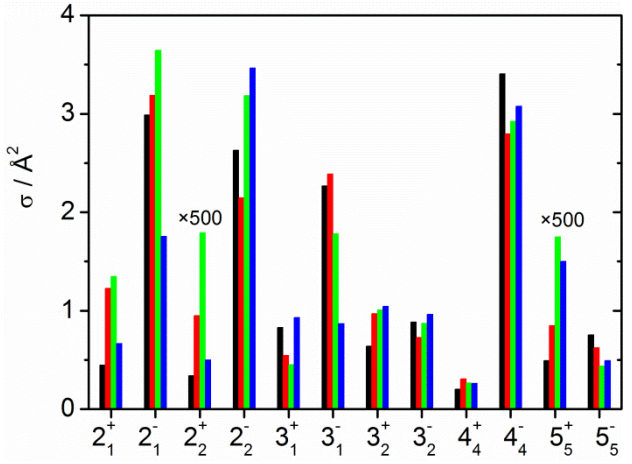

Fig. 5 Calculated integral cross sections for ND_3-He with the transformed interaction potential (black), and with the original NH_3-He (red) potential of Ref. [17] are compared with cross sections for NH_3-He (green). All calculations were performed for a collision energy of 430 cm^{-1}. The blue bars are the integral cross sections for NH_3-He from Ref. [30] at a collision energy of 436 cm^{-1}. ICSs for 2_2^+ and 5_5^+ final levels were multiplied by 500 to be visible.

with the first method. For large cross sections the differences in the ICSs calculated by the first and second method were smaller than 2%, while for the smaller cross sections the maximum difference was 10%. We found no differences in the DCSs, except for an overall scaling with the factor that we found for the ICSs. Only relative DCSs were measured, hence we used the simpler two-state ammonia inversion model for the results shown below.

In the scattering calculations the close-coupling equations were solved with the renormalized Numerov propagator, with R ranging from 4 to 40 a_0 in 212 steps. All rotational states of ND_3 up to $j = 10$ were included. For the majority of the collision energies considered here, inclusion of higher rotational levels was confirmed to result in maximum deviations of 1% for the ICSs of inelastic scattering processes to rotational levels up to $j = 7$. We took into account all partial wave contributions up to a total angular momentum of $J = 100$ and we again checked the convergence of the inelastic cross sections.

III. Results and Discussion

A. Theoretical Results

To investigate the differences between the scattering of He atoms with ND_3 and NH_3, we calculated cross sections for both isotopologues colliding with He. Moreover, we performed scattering calculations for ND_3-He with the NH_3-He interaction potential, without transforming this potential from the coordinates R, β to R', β', to investigate which changes in the ICSs are due to

differences between the potentials and which effects originate from the differences in the reduced mass and the ammonia monomer rotational constants. These calculations were performed for a collision energy of 430 cm^{-1}. The resulting ICSs for the 1_1^- initial level are shown in Figure 5, in comparison with theoretical cross sections for NH_3-He at a collision energy of 436 cm^{-1}.[30] There are significant differences in the magnitudes of

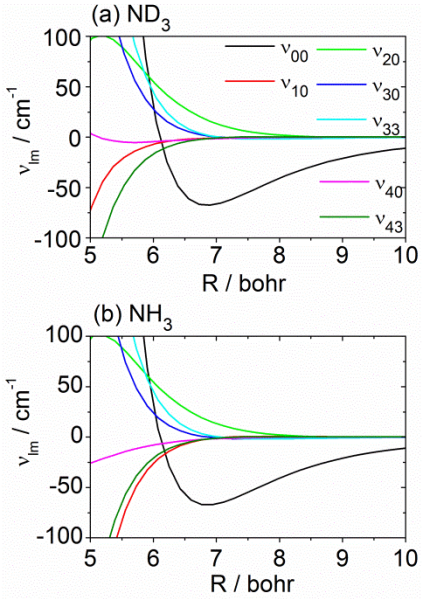

Fig. 6 Coefficients $v_{lm}(R,\rho_e)$ for the (a) ND_3-He and (b) NH_3-He interaction potential as a function of the centre-of-mass distance R, evaluated at the equilibrium ammonia umbrella angle.

the inelastic cross sections for various transitions. Moreover, the cross sections for some transitions change considerably when a different reduced mass and rotational constants or a different interaction potential are used. The variations of these changes for various state-to-state cross sections can be explained by differences in the expansion coefficients of the PES and by the relative importance of specific anisotropic terms in the expansion for transitions from the 1_1^- level to different $j'^{\pm}_{k'}$ levels.[17, 50] The most important expansion coefficients $v_{lm}(R,\rho_e)$ are plotted as a function of R at the equilibrium umbrella angle ρ_e in Figure 6 for the ND_3-He and NH_3-He interaction potentials, respectively. These expansion coefficients explain, for example, why the cross section to the 2_1^- level, which is caused in first order by the large v_{20} term, is larger than the cross section to the 2_1^+ level, which in first order is caused by the relatively small v_{10} and v_{30} terms. Note also that the cross section to the 2_2^+ level is three orders of magnitude smaller than the cross section to the 2_2^- level. This can be explained by the fact that only a combination of the v_{10} and v_{33} terms may cause a transition from the 1_1^- to the 2_2^+ level, while the large v_{33} term directly leads to the transition into the 2_2^- state.

Figure 6 also shows that the isotropic v_{00} term and the anisotropic terms in the ND_3-He and NH_3-He interaction potentials are similar, except for the v_{10}, v_{40}, and v_{43} terms. The latter terms are strongly affected by the shift of the monomer centre-of-mass, which explains the differences in the cross sections calculated for the ND_3-He system with the two different interaction potentials. The fact that these differences are substantial for some of the inelastic processes demonstrates the importance of transforming the interaction potential of NH_3-He to that for ND_3-He. The differences between the ICSs for the two systems, both calculated with the NH_3-He interaction potential, also show that the reduced mass and especially the ammonia rotational constants have a large influence on the cross sections. There are significant differences in the ICSs for NH_3-He reported

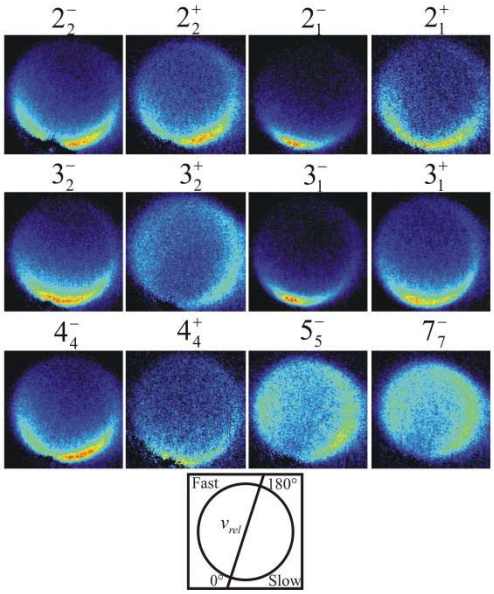

Fig. 7 Experimental velocity map images for inelastic scattering of ND_3 prepared in an initial state $j_k^{\pm} = 1_1^-$ and seeded in Ar by collision with He at a collision energy of 430 ± 40 cm^{-1}. Images are labelled by the final rotational level and +/– symmetry of the detected ND_3. The bottom panel shows a partial Newton diagram indicating the directions of the relative velocity and forward (0°) and backward (180°) scattering.

in Ref [30] and the present ones for this system. The previous *ab initio* interaction energies for NH_3-He[30] were computed using the SCF method with a (by current standards) small Gaussian basis, while the interaction energies used for the present calculations were computed with a more accurate method and larger basis set.

B. Differential cross sections for ND_3 (1_1^-) + He scattering

DCSs for collisions of ND_3 prepared in the $j_k^{\pm} = 1_1^-$ level and scattered with He into various final rotational levels were measured for three collision energies. First, the ND_3 was diluted in Ar to give a mean collision energy of 430 ± 40 cm^{-1}, for which figure 7 shows raw velocity map images. Experiments were also carried out using ND_3 seeded in Kr and Xe for which the mean collision energies were 410 ± 40 cm^{-1} and 400 ± 40 cm^{-1}, respectively. Raw images for these collision energies are shown in Supplementary Information together with a comparison of extracted and calculated DCSs. The small changes in collision energy resulting from Ar, Kr and Xe seeding of the ND_3 have no apparent effect on the scattering.

The images in Figure 7 show several distinct features. Firstly, because of conservation of energy, the state-specifically detected ND_3 products scatter on a single sphere centred at the CM of the collision and of radius proportional to the ND_3 speed, but with a small amount of blurring resulting from a distribution of molecular beam velocities and recoils imparted to the ND_3 by the

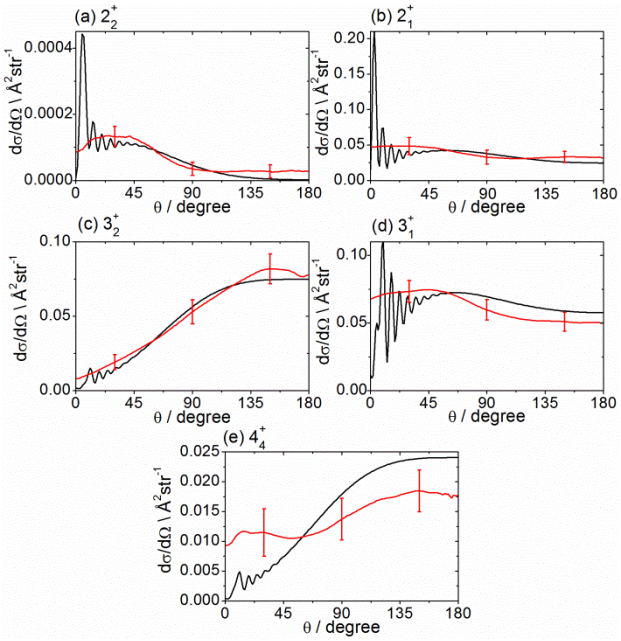

Fig. 8 DCSs for inelastic scattering of ND_3 $j_k^{\pm} = 1_1^-$ (seeded in Ar) with He into various final $j'_{k'}$ levels with + symmetry. Red lines are experimental results derived from the raw images in figure 7 following density-to-flux transformation. Black lines are QM scattering calculations. The mean collision energy was 430 ± 40 cm^{-1}.

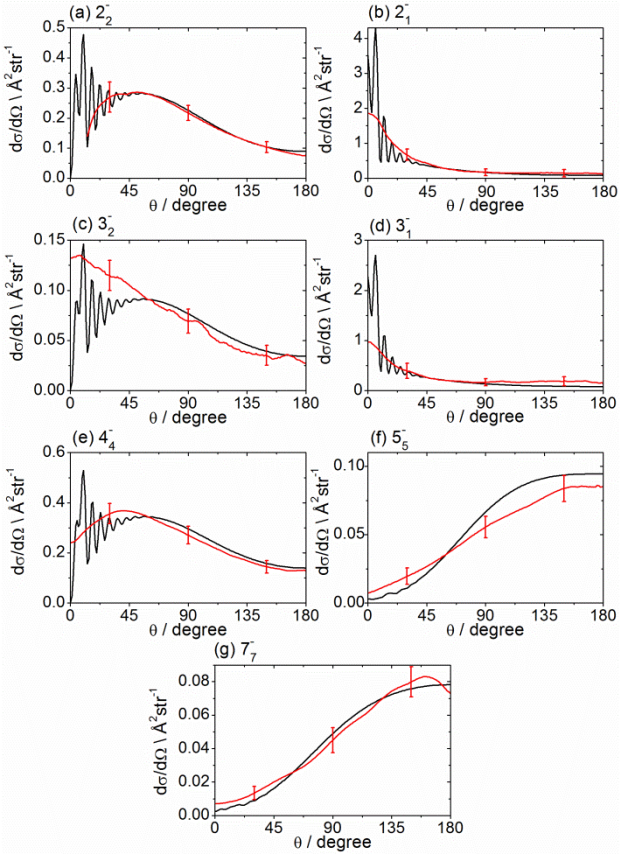

Fig. 9 DCSs for inelastic scattering of ND_3 $j_k^{\pm} = 1_1^-$ (seeded in Ar) with He into various final $j'_{k'}$ levels with − symmetry. Red lines are experimental results derived from the raw images in figure 7 following density-to-flux transformation. Black lines are QM scattering calculations. The mean collision energy was 430 ± 40 cm^{-1}.

REMPI process. The intensity at any point of the image is proportional to the number of molecules detected at the associated scattering angle, θ, and we define $\theta = 0^o$ as being parallel to the relative velocity of the ND_3 in the CM frame. Many images show a black spot in the forward direction which is a consequence of detection of trace amounts of unscattered ND_3 populating the probed rotational level within the primary molecular beam. Images accumulated with the secondary beam delayed beyond the laser firing time have been subtracted from the scattering images to give the data shown in the figures, and this subtraction can mask any scattering into the small region corresponding to the primary beam velocity in these images. Since the laser bandwidth is finite, the images have been measured only for those wavelengths where a unique assignment of a single final state is possible, with no overlapping REMPI transitions arising from other rotational levels.

DCSs extracted from the images shown in figure 7 are plotted in figures 8 and 9, with analysis using instrument functions generated from the Monte Carlo simulation as described in Section II.C. The DCSs are compared to the calculated DCSs obtained using the close-coupling method. The measured DCSs are normalized to match the values at $\theta = 60^o$ with the calculated DCSs. DCSs are not shown at small angles for certain final states, for which there is strong interference from unscattered molecules present in the parent beam. Even for those final states for which DCSs are presented over the whole range of scattering angles, the DCSs for $\theta < 10^o$ must be treated with some caution. The agreement between the experimental and calculated DCSs is in most cases good, although we are not able to resolve diffraction oscillations at small angles experimentally, because of insufficient angular resolution, which was around 15° in the forward direction.

The principal observation is that the ND_3 is forward scattered, or scattered sideways in the forward hemisphere, for product states with $j' \leq 4$, with the exception of the 3_2^+ and 4_4^+ final levels. However, for larger change in the rotational quantum number j the scattering shifts significantly into the backward hemisphere. Note also that the experiments for scattering into the highest measured rotational states (5_5 and 7_7) were performed only for – inversion symmetry, because of very weak signal for final states with + symmetry.

Some differences are observed between the DCSs for scattering into the + and − symmetry components of the same $j'_{k'}$ level. The general trend is that vibrational inversion symmetry conserving collisions are somewhat more forward scattered than the symmetry changing collisions. The most pronounced effect is seen for $j'_{k'} = 3_2$ and 4_4. In both cases, the symmetry changing collisions give DCSs peaking in the backward hemisphere, whereas the symmetry conserving collisions result in DCSs peaking in the forward hemisphere.

C. Differential cross sections for parity averaged ND_3 + He scattering

In addition to the measurements reported in the previous section for inelastic collisions of the parity selected ND_3 (1_1^-), scattering into several ND_3 rotational levels has been probed for

rotationally cooled, but not further rotational level or vibrational

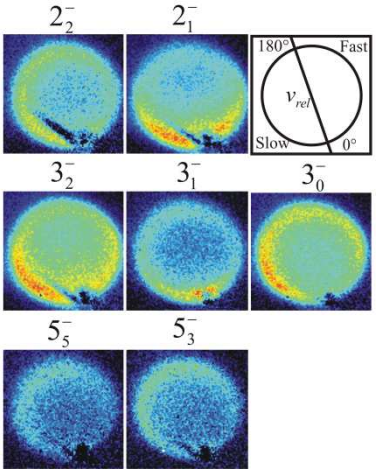

Fig. 10 Experimental velocity map images for the crossed molecular beam scattering of ND_3 (seeded in Ar) with He. The ND_3 was cooled in a supersonic expansion prior to collision with He, but was not further state-selected by a hexapole filter. The final state $j_k^{\pm} = 3_0^-$ corresponds to the A_1 nuclear spin modification and the 5_3^- level has A_1 and A_2 symmetry nuclear spin arrangements. The remaining product states have E symmetry. The collision energy was 440 ± 40 cm^{-1}.

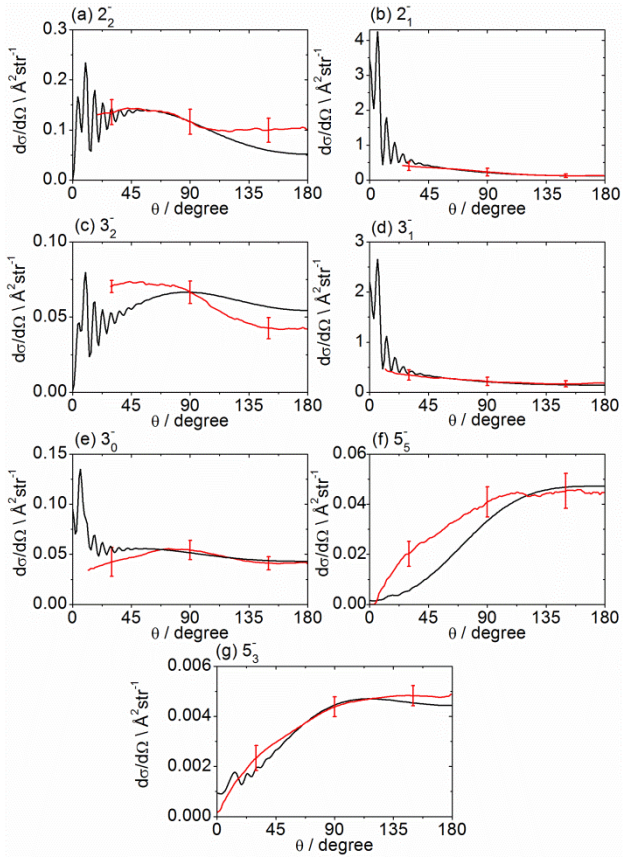

Fig. 11 DCSs for inelastic scattering of ND_3 (seeded in Ar) with helium without use of the hexapole state selector for the ND_3 beam. Red lines are experimental measurements and black lines are the results of QM scattering calculations. The mean collision energy was 440 ± 40 cm^{-1}. See the caption to Fig. 10 for nuclear spin symmetries. The umbrella vibrational inversion symmetry of the final state is – in all cases.

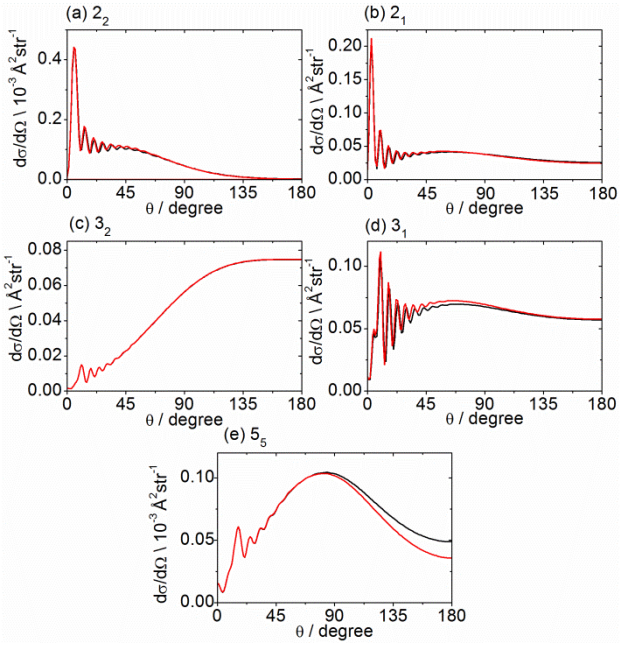

Fig. 12 Calculated differential cross sections out of the $j_k = 1_1$ level into various final levels j'_k, at a collision energy of 430 cm^{-1}. Red lines correspond to – → + vibrational inversion symmetry changes, whereas for black lines, the symmetries of the initial and final levels are reversed.

inversion symmetry selected ND_3. These experiments did not employ the hexapole state selection described in Sections II.A and B. The initial state distribution for ND_3 is shown in Table 1.

For the E nuclear spin modification, the initial state is $j_k = 1_1$, but +/– symmetry averaged, whereas the initial states for A_1 are $j_k^{\pm} = 0_0^+$ and 1_0^- and for the A_2 modification are $j_k^{\pm} = 0_0^-$ and 1_0^+. State selective detection was carried out solely through the $\tilde{B}(5)$ band, therefore the inversion symmetry of the final level for all measured images is –. The velocity map images and the DCSs extracted from them following density-to-flux transformation are shown in figures 10 and 11. The final state 3_0^- corresponds to the A_1 nuclear spin modification and the 5_3^- level has components with symmetries A_1 and A_2. The remainder of the measured images correspond to the E nuclear spin modification. Again, there is good agreement between experimental data and the DCSs obtained from QM scattering calculations.

Scattering of the ND_3 in the E nuclear spin modification prepared without hexapole parity selection (initial level 1_1) into 2_1^-, 2_2^-, 3_1^-, 3_2^- and 5_5^- states can be compared to the corresponding results for parity selected ND_3 (1_1^-) reported in section III.B. In this way, the scattering out of the 1_1^+ initial level may be explored. All these DCSs measured with the inversion symmetry averaged initial state (1_1) are in quantitative agreement with corresponding DCSs measured for the symmetry selected initial state (1_1^-), suggesting at most a minor contribution from the scattering from the 1_1^+ level into a given final j'^-_k, state. This deduction is supported by the theoretical calculations, which reveal that the ICSs for scattering out of the 1_1^+ level into final levels with - symmetry are much smaller than for the 1_1^- level. Calculated DCSs out of the 1_1^+ level into various final levels with – inversion symmetry are almost identical to the DCSs out of the 1_1^- initial level to the same final levels, but with + symmetry, as shown in Figure 12.

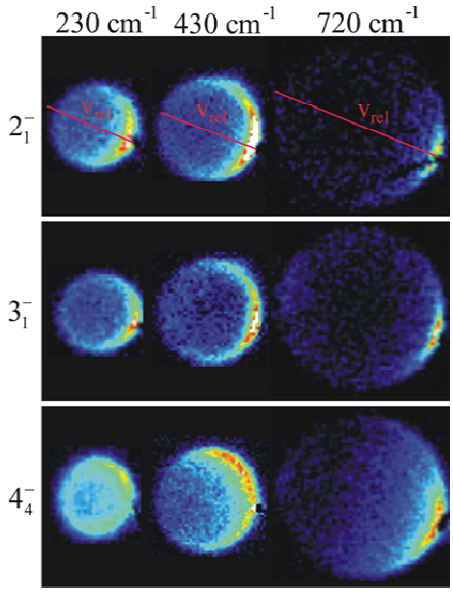

Fig. 13 Experimental velocity map images for inelastic scattering of ND_3 prepared in an initial state $j_k^{\pm} = 1_1^-$ and seeded in Ar by collision with He at collision energies of 230, 430 and 720 cm^{-1}. Images are labelled by the final rotational level and – symmetry of the detected ND_3. The directions of the relative velocity vectors are shown in the top panel.

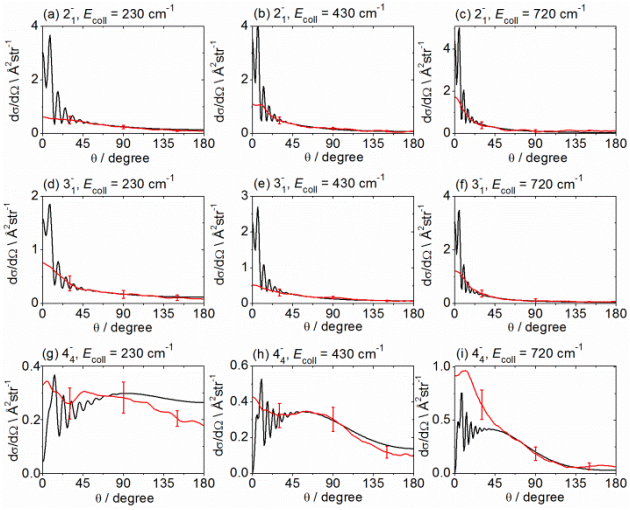

Fig. 14 DCSs for inelastic scattering of hexapole state-selected ND_3 $j_k^{\pm} = 1_1^-$ (seeded in Ar) with He into the 4_4^- state for the various collision energies indicated. Experimental results determined from density-to-flux transformation of raw velocity map images (red lines) are compared to quantum scattering calculations (black lines).

D. Dependence of the differential cross section on the collision energy

Seeding the ND_3 in either excess Kr or Xe carrier gas instead of Ar gave small variations in the mean collision energy: the ND_3 (in Kr) + He and ND_3 (in Xe) + He collision energies were respectively 410 ± 40 cm^{-1} and 400 ± 40 cm^{-1}, compared to 430 ± 40 cm^{-1} for ND_3 seeded in Ar. However, the effects of these changes proved negligible, as shown by data presented in the Supplementary Information. One consequence of this outcome is that experimental data obtained with a ± 40 cm^{-1} spread of collision energies can be compared with computational results at a single mean collision energy without the need for convolution over the experimental distribution.

More significant changes to the collision energy required use of a different molecular beam apparatus in which the intersection angle between ND_3 (in Ar) and He beams could be changed from 90°. Velocity map images acquired for He + ND_3 $(1_1^-) \rightarrow$ He + ND_3 (2_1^-, 3_1^- and 4_4^-) state-to-state scattering at collision energies of 230, 430 and 720 cm^{-1} are shown in figure 13. The image analysis with appropriate modifications to the density-to-flux transformation code (in this case, requiring use of the IMSIM program) to accommodate changes to the experimental geometry gave the DCSs plotted in figure 14. The experimental DCSs were normalized to match a value at θ = 70°. The measured DCSs are more sharply forward peaking as the collision energy increases from 230 to 720 cm^{-1}. The most pronounced change in the angular distribution with increasing collision energy is seen for the 4_4^- final level. These DCSs show a pronounced shift from a broad distribution extending over the entire angular range to sharp forward scattering as the collision energy increases from 230 to 720 cm^{-1}, indicating that longer range interactions are sufficient at the higher collision energies to induce Δj = +3 and Δk = +3 changes to the rotational angular momentum. The sensitivity of the DCSs to the collision energy must reflect the changes in the impact-parameter dependence of the torque applied to the ND_3 that is required to produce the final levels as the collision energy increases.

IV. Conclusions

Comparison of fully state-to-state differential cross sections for inelastic scattering of ND_3 $(\tilde{X},v = 0, j_k^{\pm} = 1_1^-)$ with He at a collision energy of 430 cm^{-1} shows very satisfactory agreement between experimental measurements and quantum mechanical scattering calculations performed with an *ab initio* potential energy surface. The comparisons are made for final rotational levels up to $j'_{k'} = 7_7$ and for both symmetric (+) and antisymmetric (–) components of the inversion vibration associated with the ν_2 umbrella mode of ND_3. The experimental DCSs were derived from velocity map images obtained using a crossed molecular beam machine. Image processing required careful treatment of the transformation from density to flux to compensate for experimental bias towards detection of products with lower laboratory frame speeds.

For small changes in the j rotational angular momentum quantum number, the ND_3 is predominantly forward scattered at a mean collision energy of 430 cm^{-1}, but the scattering shifts to the sideways and backward directions as Δj increases. A simple interpretation of these observations is that smaller impact parameter collisions are required to generate a greater torque on the ND_3. The DCSs also differ for scattering from the initial 1_1^- state to $j'_{k'}$ levels with the same j' and k' values but different + or – symmetries with respect to the vibrational inversion motion. All these effects are captured quantitatively by the QM scattering calculations, lending considerable confidence to the quality of the PES employed and the validity of a reduced dimensionality

treatment of the degrees of freedom of the ND_3. Further investigation of the He + ND_3 (1_1^-) → He + ND_3 (2_1^-, 3_1^- and 4_4^-) state-to-state scattering reveals DCSs that are very sensitive to the collision energy in the range 230 – 720 cm^{-1}. Experimental and computational studies are now underway to test whether the agreement we observe between velocity map imaging and quantum mechanical scattering calculation results for ND_3 + He collisions is replicated for other collision partners such as H_2, and Ar.

Acknowledgements

The Nijmegen group acknowledges financial support from NWO-CW ECHO (for A.S.) and the EU Marie-Curie Initial Training Network *Molecular Universe* (for C.-H.Y.). The Bristol group thanks EPSRC for funding via the EPSRC Programme Grant EP/G00224X. Both groups are part of the EU Initial Training Network *ICONIC* which provided financial support for C.B. and O.T. and for visits between the two institutions. S.Y.T.v.d.M. acknowledges support from NWO via a VIDI grant.

Notes and references

[a] *School of Chemistry, University of Bristol, Cantock's Close, Bristol BS8 1TS, UK; E-mail: a.orr-ewing@bris.ac.uk*
[b] *Radboud University Nijmegen, Institute for Molecules and Materials, Toernooiveld 1, 6525ED Nijmegen, The Netherlands; E-mail: parker@science.ru.nl, avda@theochem.ru.nl*

† Electronic Supplementary Information (ESI) available: the ESI contains images measured at different collision energies and plots of extracted DCSs in comparison with computed DCSs. See DOI: 10.1039/b000000x/

1. U. Machin and E. Roueff, Journal of Physics B-Atomic Molecular and Optical Physics, 2005, **38**, 1519-1534.
2. W. F. Wang, Chemical Physics, 2003, **288**, 23-31.
3. A. C. Cheung, D. M. Rank, C. H. Townes, D. D. Thornton and W. J. Welch, Physical Review Letters, 1968, **21**, 1701-&.
4. N. Biver, D. Bockelee-Morvan, J. Crovisier, A. Lecacheux, U. Frisk, A. Hjalmarson, M. Olberg, H.-G. Floren, A. Sandqvist and S. Kwok, Planetary and Space Science, 2007, **55**, 1058-1068.
5. T. Handa, T. Omodaka, T. Nagayama, H. B. Iahak and N. Matsuyama, in Galactic Center Workshop 2006: From the Center of the Milky Way to Nearby Low-Luminosity Galactic Nuclei, ed. B. G. C. Schodel R., Muno M. P., Nayakshin S. O. T., 2006, vol. 54, pp. 42-46.
6. D. Saumon, M. S. Marley, M. C. Cushing, S. K. Leggett, T. L. Roellig, K. Lodders and R. S. Freedman, Astrophysical Journal, 2006, **647**, 552-557.
7. H. S. Liszt, R. Lucas and J. Pety, Astronomy & Astrophysics, 2006, **448**, 253-259.
8. A. B. Burgess, A. Dudhia, R. G. Grainger and D. Stevenson, in Atmospheric Remote Sensing: Earth's Surface, Troposphere, Stratosphere and Mesosphere, eds. J. P. Burrows, K. U. Eichmann and E. J. Lewellyn, 2006, vol. 37, pp. 2218-2221.
9. D. Sudarsky, A. Burrows and I. Hubeny, Astrophysical Journal, 2003, **588**, 1121-1148.
10. E. Roueff, D. C. Lis, F. F. S. van der Tak, M. Gerin and P. F. Goldsmith, Astronomy & Astrophysics, 2005, **438**, 585-598.
11. A. C. Cheung, D. M. Rank, C. H. Townes and W. J. Welch, Nature, 1969, **221**, 917-&.
12. R. Mauersberger, C. Henkel and T. L. Wilson, Astronomy and Astrophysics, 1987, **173**, 352-360.
13. C. M. Walmsley and H. Ungerechts, Astronomy and Astrophysics, 1983, **122**, 164-170.
14. S. Guilloteau, T. L. Wilson, R. N. Martin, W. Batrla and T. A. Pauls, Astronomy and Astrophysics, 1983, **124**, 322-325.
15. B. H. Yang and P. C. Stancil, European Physical Journal D, 2008, **47**, 351-358.
16. J. Schleipen and J. J. ter Meulen, Chemical Physics, 1991, **156**, 479-496.
17. K. B. Gubbels, S. Y. T. van de Meerakker, G. C. Groenenboom, G. Meijer and A. van der Avoird, Journal of Chemical Physics, 2012, **136**.
18. G. C. M. van der Sanden, P. E. S. Wormer and A. van der Avoird, Journal of Chemical Physics, 1996, **105**, 3079-3088.
19. H. Meyer, J. Phys. Chem. A, 1995, **99**, 1101-1114.
20. S. Bosanac, Phys. Rev. A, 1980, **22**, 2617-2622.
21. H. Meyer, Mol. Phys., 1995, **84**, 1155-1178.
22. N. Yonekura, C. Gebauer, H. Kohguchi and T. Suzuki, Review of Scientific Instruments, 1999, **70**, 3265-3270.
23. M. L. Vestal, C. R. Blakley, P. W. Ryan and J. H. Futrell, Review of Scientific Instruments, 1976, **47**, 15-26.
24. P. Jansen, D. W. Chandler and K. E. Strecker, Rev. Sci. Instrum., 2009, **80**, 083105.
25. A. Eppink and D. H. Parker, Rev. Sci. Instrum., 1997, **68**, 3477-3484.
26. O. Tkáč, A. G. Sage, S. J. Greaves, A. J. Orr-Ewing, P. J. Dagdigian, Q. Ma and M. H. Alexander, Chem. Sci., DOI:10.1039/C3SC52002A, 2013.
27. Z. R. Li, A. Chou and F. M. Tao, Chemical Physics Letters, 1999, **313**, 313-320.
28. M. P. Hodges and R. J. Wheatley, Journal of Chemical Physics, 2001, **114**, 8836-8843.
29. H. Meyer, U. Buck, R. Schinke and G. H. F. Diercksen, J. Chem. Phys., 1986, **84**, 4976-4987.
30. G. C. M. van der Sanden, P. E. S. Wormer, A. van der Avoird, J. Schleipen and J. J. ter Meulen, Journal of Chemical Physics, 1995, **103**, 10001-10004.
31. G. D. Billing, L. L. Poulsen and G. H. F. Diercksen, Chemical Physics, 1985, **98**, 397-408.
32. S. L. Davis, J. E. Boggs and S. C. Mehrotra, Journal of Chemical Physics, 1979, **71**, 1418-1425.
33. B. Yan, P. F. H. Claus, B. G. M. van Oorschot, L. Gerritsen, A. T. J. B. Eppink, S. Y. T. van de Meerakker and D. H. Parker, Review of Scientific Instruments, 2013, **84**, 023102.
34. R. Locht, B. Leyh, W. Denzer, G. Hagenow and H. Baumgartel, Chemical Physics, 1991, **155**, 407-422.
35. L. Duggan, M. Raunhardt, M. Schaefer, U. Hollenstein, T. P. Softley and F. Merkt, Molecular Physics, 2010, **108**, 1069-1082.
36. D. H. Parker, R. F. Delmdahl, B. Bakker and H. P. Loock, Journal of the Chinese Chemical Society, 2001, **48**, 327-332.
37. M. N. R. Ashfold, S. R. Langford, R. A. Morgan, A. J. Orr-Ewing, C. M. Western, C. R. Scheper and C. A. de Lange, The European Physical Journal D - Atomic, Molecular, Optical and Plasma Physics, 1998, **4**, 189-197.
38. C. M. Western, in PGOPHER, a Program for Simulating Rotational Structure, University of Bristol, 7.1.108 edn., 13 Sep 2010
39. N. M. R. Ashfold, R. N. Dixon, R. J. Stickland and C. M. Western, Chemical Physics Letters, 1987, **138**, 201-208.
40. J. Bentley, B. J. Cotterell, A. Langham and R. J. Stickland, Chemical Physics Letters, 2000, **332**, 85-92.
41. M. N. R. Ashfold, R. N. Dixon, N. Little, R. J. Stickland and C. M. Western, Journal of Chemical Physics, 1988, **89**, 1754-1761.
42. G. C. McBane, in IMSIM computer program, version 1.4, The Ohio State University, 1999.
43. C. J. Eyles, Ph. D. thesis, University of Oxford, 2010.
44. C. J. Eyles, M. Brouard, H. Chadwick, B. Hornung, B. Nichols, C. H. Yang, J. Kłos, F. J. Aoiz, A. Gijsbertsen, A. E. Wiskerke and S. Stolte, Phys. Chem. Chem. Phys., 2012, **14**, 5403-5419.
45. C. J. Eyles, M. Brouard, C. H. Yang, J. Klos, F. J. Aoiz, A. Gijsbertsen, A. E. Wiskerke and S. Stolte, Nature Chemistry, 2011, **3**, 597-602.
46. G. C. McBane, Simulation of crossed beam images (in Imaging in Chemical Dynamics), ACS Books, 2001.

47. S. Antonova, A. Lin, A. P. Tsakotellis and G. C. McBane, Journal of Chemical Physics, 1999, **110**, 11742-11748.
48. K. T. Lorenz, D. W. Chandler and G. C. McBane, Journal of Physical Chemistry A, 2002, **106**, 1144-1151.
49. V. M. Devi, P. P. Das, K. N. Rao, S. Urban, D. Papousek and V. Spirko, Journal of Molecular Spectroscopy, 1981, **88**, 293-299.
50. J. Millan, N. Halberstadt, G. C. M. van der Sanden and A. van der Avoird, Journal of Chemical Physics, 1995, **103**, 4138-4149.